Biophysical Journal
Article

Biophysical Society

The Effect of Cortical Elasticity and Active Tension on Cell Adhesion Mechanics

Bart Smeets,[1,*] Maxim Cuvelier,[1] Jiri Pešek,[1] and Herman Ramon[1]
[1]MeBioS, KU Leuven, Heverlee, Belgium

ABSTRACT We consider a cell as an elastic, contractile shell surrounding a liquid incompressible cytoplasm and with nonspecific adhesion. We perform numerical simulations of this model to study the mechanics of cell-cell separation. By variation of parameters, we are able to recover well-known limits of the Johnson-Kendall-Roberts theory, the Derjaguin-Muller-Toporov model, adhesive vesicles with surface tension (Brochard-Wyart and de Gennes derivation), and thin elastic shells. We further locate biological cells on this parameter space by comparison to existing experiments on S180 cells. Using this model, we show that mechanical parameters can be obtained that are consistent with both dual pipette aspiration and micropipette aspiration, a problem not successfully tackled so far. We estimate a cortex elastic modulus of $E_c \approx 15$ kPa, an effective cortex thickness of $t_c \approx 0.3\ \mu$m, and an active tension of $\gamma \approx 0.4$ nN/μm. With these parameters, a Johnson-Kendall-Roberts-like scaling of the separation force is recovered. Finally, the change of contact radius with applied force in a pull-off experiment was investigated. For small forces, a scaling similar to both the Brochard-Wyart and de Gennes derivation and the Derjaguin-Muller-Toporov model is found.

INTRODUCTION

The mechanical response of a cell to deformation arises from the properties of the underlying cytoskeleton. The intricate dynamic structure and active nature of the actomyosin cortex produce complex time-dependent behavior, including a power-law-creep response (1) and nonlinear soft glassy rheology (2). This complicates mechanical measurements on cells because the parameterization of experimental results is often not invariant with respect to the conditions of the experiment. Still, simplified mechanical models may be adopted in the relevant spatiotemporal limits (3). For example, at long timescales, cells behave as Newtonian liquid drops under surface tension—"cortical shell-liquid core" model (4,5)—whereas at short timescales and small deformations, the cell is elastic—"solid elastic sphere" model—with a characteristic Hertzian force upon indentation (6).

When applying these limits to micropipette aspiration (MA) experiments, the cell's resistance to deformation is expressed either as a cortex tension or as a solid cell Young's modulus E_{cell}. Extending from this, Chu et al. used dual pipette aspiration (DPA) experiments in controlled adhesion conditions to demonstrate how cell-cell pull-off forces compare to various limiting continuum theories, thereby indirectly probing the mechanical properties of suspension cells (7). For the cortical shell-liquid core model, the pull-off force required to separate two droplets with net adhesion energy w was derived by Brochard-Wyart and de Gennes (BWdG) as $F_s = \pi \widehat{R} w$ (8), with $\widehat{R} = R_1 R_2/(R_1 + R_2)$. For solid elastic spheres, Johnson-Kendall-Roberts (JKR) theory predicts the pull-off force in the limit of short range of adhesive interaction and soft spheres as $F_s = 3/2\pi \widehat{R} w$ (9). In the opposite limit of stiff spheres with a large adhesive range, the model of Derjaguin-Muller-Toporov (DMT) predicts a pull-off force $F_s = 2\pi \widehat{R} w$ (10,11). For S180 cells, it was found that the pull-off force scales as $F_s \sim \frac{3}{2}\pi \widehat{R} w$, consistent with the JKR model for adhesion between solid elastic asperities but not with the BWdG expression for adhesive droplets with surface tension (7). This suggests that a solid elastic model is an appropriate description of the cell in these conditions (suspension, short timescale). Yet, there is an apparent mismatch between the elastic modulus estimated from such a pull-off experiment using JKR theory and the Young's modulus obtained from a simple single-cell aspiration experiment (12). For example, on S180 murine sarcoma cells, a Young's modulus (only the composed modulus $\widehat{E}_{\mathrm{cell}} = E_{\mathrm{cell}}/[2(1-\nu_{\mathrm{cell}}^2)]$ can be estimated this way) $E_{\mathrm{cell}} > 1$ kPa is obtained from applying JKR theory to a DPA experiment (7), whereas single-cell aspiration tests (MA) on the same cell line yield a much

Submitted June 13, 2018, and accepted for publication January 17, 2019.

*Correspondence: bart.smeets@kuleuven.be

Editor: Jennifer Curtis.

https://doi.org/10.1016/j.bpj.2019.01.015

lower modulus of $E_{cell} \approx 100$ Pa (12), even though both experiments are performed in similar conditions and at comparable timescales (seconds). (A value of $E_{cell} \approx 100$ Pa is obtained when applying the analysis for elastic spheres (4) to the critical pressure that corresponds to the net tension of 0.9 nN/μm that was reported in (12). Note that only the order-of-magnitude of E_{cell} suffices for the argument provided.)

One obvious explanation is that the mechanical rigidity of a suspension cell is mostly concentrated in an elastic cortical shell rather than uniformly distributed throughout the cell. Thin elastic shell models have been frequently applied to cells, e.g., for analyzing the shape of blebbing (13), bulging (5), or dividing cells (14). For adhering curved elastic shells, an expression for the pull-off force as a function of Young's modulus E_c, Poisson number ν_c, and thickness t_c has been derived in (15):

$$\left(\frac{F_s}{P*}\right)^3 = \frac{w^4 \widehat{R}^4 \left(1-\nu_c^2\right)}{E_c t_c^2}. \quad (1)$$

$P*$ is a dimensionless scaling factor that depends on the load conditions—for fixed load, $P* \approx 13.2$ (15). When applying this equation to cells, E_c refers to the Young's modulus of the thin actin cortex that surrounds the cytosolic interior. A typical cell's actomyosin cortex has a thickness of roughly 200 nm and a Young's modulus on the order of 10 kPa (16). Within this range of properties and for a characteristic adhesion energy of $w \approx 1$ nN/μm and a cell size of $\widehat{R} \approx 5$ μm, it can be verified using Eq. 1 that for a shell, the pull-off force $F_s \gg 2\pi\widehat{R}w$, i.e., much greater than what was measured in (7). In other words, although the cell's cytoskeletal structure resembles a thin shell, it behaves more like a solid elastic asperity during pull-off.

This discrepancy could be attributed to the highly nonlinear and anisotropic behavior of the cortical actomyosin and microtubule network (17,18). As such, its "effective" mechanical thickness would be significantly higher than the thickness measured using optical methods (16,19,20). This explanation is in line with observations of cortical rheology at long timescales, at which a considerably elevated effective thickness is required to recover the rate of cell spreading using a simple Newtonian liquid model (21).

A second possible explanation lies in the active nature of the cortex: contractility induced by myosin II motors generates an active tension (γ), which counterbalances adhesion and thereby assists in the separation of two cells. For mature intercellular junctions, it has been shown that even the local regulation of contractility at the cell-cell interface rather than adhesion itself controls the extent of contact expansion. Then, the role of adhesion molecules is restricted to the mechanical anchoring of the cortex (5). Although this local regulation of cortical tension is unlikely to affect adhesive behavior in controlled adhesion experiments at very short timescales (seconds), the total (uniform) cortical tension is likely to play a major role in a pull-off experiment. It should be noted here that this active tension is not the same as the surface tension often reported from mechanical tests (4,12,16), in which a liquid model is used that assumes that no elastic stresses are present. This assumption can be valid at long timescales, when remodeling of the cortex effectively relaxes all elastic stresses. In the absence of this relaxation, these two quantities would only coincide in the limit of a soft/thin cortex (see further).

Here, we propose a numerical model that tries to reconcile the aforementioned observations, describing adhesive contact between cells as a function of the elastic properties of the cell's acto-myosin cortex and its active contractility. Cells are represented as spherical elastic shells that maintain internal volume and for which adhesive/repulsive contact is described using a Dugdale approach (22). Active contractility is explicitly introduced through a contractile tension and acts similarly to an additional surface tension (see Fig. 1). Using this model, we show how different scaling laws for a pull-off experiment can be recovered by changing the stiffness E_c, effective thickness t_c, and the active tension γ of the cortex. Next, in a case study on S180 suspension cells, we demonstrate how JKR-like behavior can be recovered during pull-off while remaining consistent to single-cell MA experiments. Doing so allows us to estimate the (instantaneous) mechanical properties of the S180 cell cortex.

METHODS

Computational model

We introduce a dynamical model that represents the cells as a triangulated spherical shell. This shell represents the cortex-membrane complex, wherein the actin cortex accounts for the majority of its mechanical rigidity (13), see Fig. 1. Overdamped equations of motion $\Lambda\, x = F$ are solved to obtain the positions x, representing the nodes from a triangulated shell. Viscous (velocity-dependent) forces are represented in the resistance matrix Λ, whereas all other forces are assembled on the right-hand side in F. A shell model for linear viscoelasticity (Young's modulus E_c, Poisson number

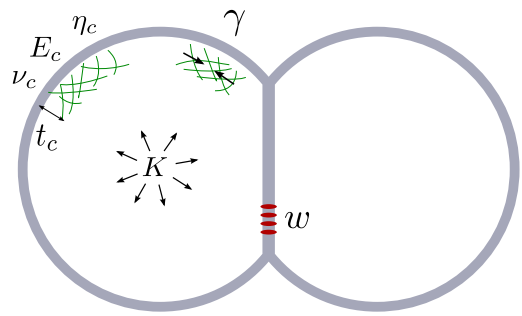

FIGURE 1 Schematic representation of a doublet of adhering cells: the cell's cortex with thickness t_c has passive elastic properties (Young's modulus E_c, Poisson ratio ν_c, and viscosity η_c) and an active contractile tension γ. Volume is maintained through a bulk modulus K, and adhesion energy w drives the formation of initial cell-cell contacts. To see this figure in color, go online.

ν_c, thickness t_c, and viscosity η_c) is implemented in a spring-damper network (see Supporting Materials and Methods, Section 1), in which for simplicity we have assumed that $\nu_c = 1/3$ (the Poisson's ratio of a two-dimensional isotropic system is 1/3 if the constituents (nodes) interact with central forces that depend on distance alone (23)). To introduce active tension γ and conservation of volume with bulk modulus K, a local outward pressure is computed as

$$p(x) = 2\gamma\left(\frac{1}{R} - \frac{1}{r_c(x)}\right) - K\frac{V - V^*}{V^*}, \qquad (2)$$

for a cell with radius R, volume V, and initial volume V^*. $r_c(x)$ is the local mean radius of curvature on the cell surface at position $\vec{x}$. We assume cell volume changes are negligible at the relevant timescale (13) and set $K =$ 30 kPa, a value sufficiently high to prevent significant changes of cell volume during MA and DPA simulations—see Fig. S7. The cell's surface is decorated with nonspecific stickers, which are assumed to be fixed and uniformly distributed on the cell and equal for both cells, leading to a work of interaction $w = w_1 + w_2$.

We aim to describe adhesive behavior in a wide range of cortical thickness. For larger t_c and low E_c, the normal (radial) elastic deformation of the cortex cannot be neglected anymore. Therefore, we use a modified Maugis-Dugdale contact model (22) that formulates a Hertzian repulsive pressure based on the contact stiffness, an adhesive traction based on the adhesion energy w, and an effective range of interaction h_0. For solid elastic spheres, the latter parameter captures the transition between the JKR (low h_0) and the (DMT) limit (high h_0)—for an in-depth review, see (11). For cells, the effective adhesive range is typically small and well in the JKR zone, and we set $h_0 = 50$ nm (24). Because the Hertzian repulsive model is valid for a "solid" elastic asperity, a requirement of this contact model is that the normal elastic compression of the cortex is small compared to its thickness. A discussion on the limitations of this model is provided in the Conclusions, and a detailed description of the full computational methodology is presented in the Supporting Materials and Methods, Sections 1 and 2.

Simulation setup

Setups are created for numerical simulation of two mechanical tests: MA and DPA. For MA, we include an idealized pipette with a tip of toroidal shape of inner radius $R_p = 3.5$ μm (12)—see Fig. 2 *a* and Supporting Materials and Methods. Within the pipette, an aspiration pressure P_a is applied normal to the cell surface. For DPA, we first let two cells freely adhere until their contact area reaches a steady value—Fig. 2 *b*. Next, a pulling force is distributed—see Supporting Materials and Methods—to the nodes of both cells ($-F_p$ and F_p). We record the contact radius R_c while the pulling force is gradually increased until the cells suddenly lose contact—Fig. 2 *c*. The force at which this occurs is registered as the separation force F_s. Further details and numerical considerations of the simulation setup are provided in the Supporting Materials and Methods.

RESULTS

Pull-off force in cell model

First, we show in general how the separation force depends on the mechanical properties of the cell's cortex. For this, we define a dimensionless thickness as $\kappa := \sqrt{\widehat{E}/(\widehat{R}w)}\, t_c$. This chosen normalization is a "rigidity" measure that ensures that a unique normalized separation force $\overline{F}_s := F_s/\pi\widehat{R}w$ is found for the limits of BWdG ($\overline{F}_s = 1$), JKR ($\overline{F}_s = 3/2$), DMT ($\overline{F}_s = 2$), and shells—Eq. 1—upon change of κ. Here, we are mainly interested in the role of the effective cortical thickness t_c and active tension γ.

Fig. 3 shows $\overline{F}_s$ as a function of κ by varying t_c for a simulated DPA experiment. Traversing from high κ (*right*) to low κ (*left*), four regions of distinct behavior can be recognized in these curves: 1) at high κ or for contact radius $R_c \ll t_c$, adhesion is dominated by localized elastic deformation normal to the contact plane. Here, solid-sphere Maugis-Dugdale adhesion is recovered, and $\overline{F}_s$ will range from the JKR to the DMT limit; 2) for lower κ, or $t_c \ll R_c \ll \widehat{R}$, the contribution of bending resistance is dominant (bending rigidity $k_b \sim t_c^3$). This resistance to curvature change is similar to surface tension: the BWdG limit $\overline{F}_s = 1$ is approached; 3) as κ decreases, a sharp increase in $\overline{F}_s$ is observed, similar to shell theory. The adhesion energy is balanced by in-plane elastic energy distributed over the complete cortex; 4) at very low κ, the complete cortex is

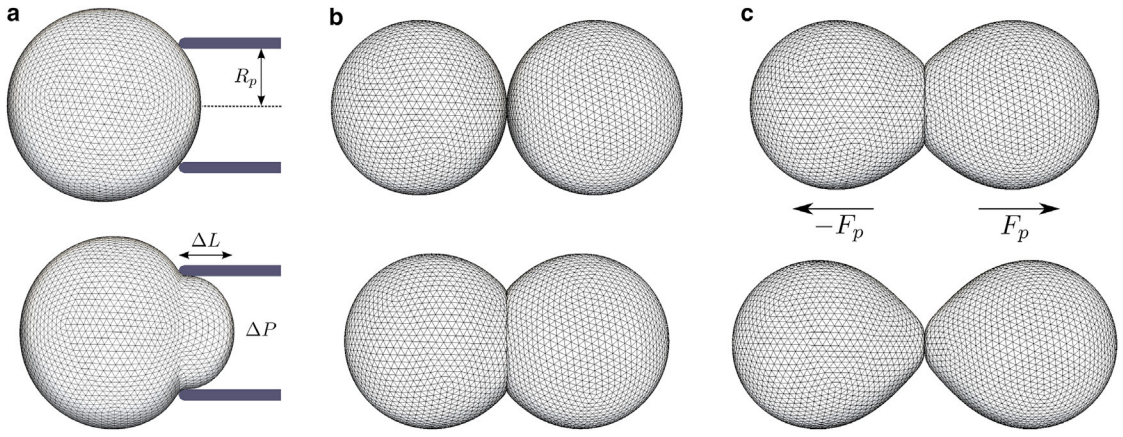

FIGURE 2 Visualization of simulation setups for MA and DPA experiments. (*a*) Simulation of MA experiment. An underpressure ΔP is applied within a micropipette of radius R_p (*top*). The pressure is gradually increased (*bottom*) until the aspirated length $\Delta L = R_p$. At this point, the pressure is registered as the critical pressure P_c. (*b*) Simulation of cell-cell adhesion. Two cells are brought in close proximity (*top*) and allowed to naturally adhere (*bottom*). (*c*) Simulation of DPA experiment, starting from a doublet of adhering cells. A pulling force F_p is applied on the cells (*top*) and gradually increased until rapid separation occurs (*bottom*). At this point, the pulling force is registered as the separation force F_s. To see this figure in color, go online.

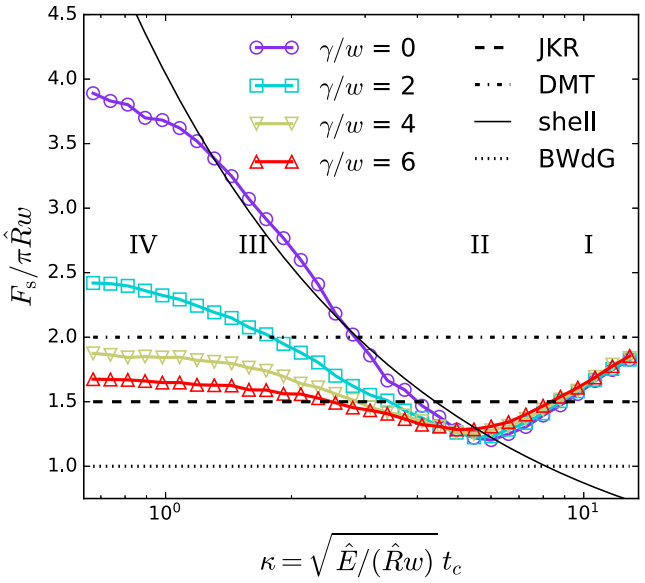

FIGURE 3 Normalized pull-off force $F_s/\pi\widehat{R}w$ as a function of dimensionless thickness κ for varying active tension γ. The simulations were obtained by varying thickness t_c while $\widehat{R} = 5$ μm, $E = 25$ kPa, and $w = 0.25$ n N/μm. For reference, the pull-off force from JKR, DMT, BWdG, and shell theory is shown for these parameters. To see this figure in color, go online.

under high strain, and shell theory breaks down. A maximal contact radius R_c on the order of $\widehat{R}$ is reached, and volume conservation (bulk modulus K) limits further deformation. A plateau is observed at large values of $\overline{F}_s$. It should be noted that the proposed computational description becomes invalid at both extremes of κ. At very large κ, the thin-shell assumption of cortex elasticity breaks down. At low κ, indentations will become large compared to thickness, and the assumptions of our adhesion model break down. Although this can be safely mitigated by replacing the normal contact stiffness with a sufficiently stiff constraint, the system becomes prone to buckling instabilities in the absence of active tension. Unsurprisingly, the role of active tension γ is mainly significant at small values of κ, at which it reduces $\overline{F}_s$ toward the JKR-DMT zone. Given what we know about typical mammalian cells (see Introduction), we expect κ to be small, even if an "effective" thickness would be much greater than the optical thickness. In this case, a significant cortical tension is required for a pull-off force to be in the JKR-DMT zone, $3/2 \leq \overline{F}_s \leq 2$.

Case study on S180 cells

We try to locate cells in this general framework by considering S180 cells, a mechanically very well-investigated cell line. In Chu et al. (7), pull-off forces were measured using DPA in controlled adhesion experiments. We have replotted these results in Fig. 4 *a*. A scaling of $\overline{F}_s$ in the region of the JKR and DMT limits can be observed, with an average $\overline{F}_s \approx 1.75$ in the sampled region of w. In our model, such a scaling could be obtained for many possible combinations of E_c, t_c, and γ. To restrict the parameter space to realistic cell properties, we first compare our results to separate MA experiments on the same cell line. In Engl et al. (12), a (liquid model) mean cortical tension of 0.9 n N/μm was found (this value of 0.9 n N/μm already gives an upper limit for estimates of the active tension γ that should be approached in the limit of a soft and thin elastic shell) from MA on S180 cells, which corresponds to a critical pressure $P_c \approx 250$ Pa. We sampled combinations of E_c, t_c, and γ in a full factorial $15 \times 15 \times 15$ grid and performed MA simulations to compute the critical pressure (see Supporting Materials and Methods, Section 2). From this, an isosurface was extracted that represents all parameter combinations, yielding a critical pressure of 250 Pa—Fig. 4 *b*. Subsequently, we resampled points in a regular distribution on this isosurface. Each of these points represents a combination of E_c, t_c, and γ that resembles the mechanical behavior of an (average) S180 cell in an MA experiment.

Finally, we performed simulations of DPA on these new samples at an intermediate $w = 0.5$ n N/μm and registered $\overline{F}_s$. The result of this can be seen in Fig. 4 *b*. The lower values of $1.5 \leq \overline{F}_s \leq 2$ observed in (7) occur only at lower E_c, when additional resistance to deformation is offered by either bending rigidity (at higher t_c) or active tension

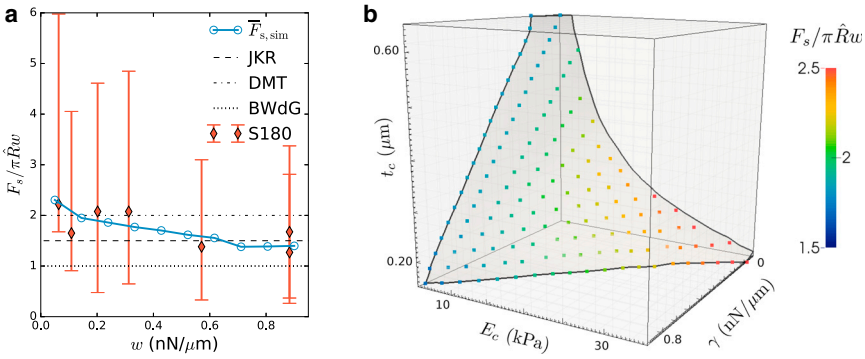

FIGURE 4 (*a*) Normalized DPA pull-off force $F_s/\pi\widehat{R}w$ as a function of dextran-depletion-induced adhesion w between S180 cells, replotted from Fig. 2 in Chu et al. (7) (*red diamonds*), together with simulated DPA experiment at $E_c = 15$ kPa, $t_c = 0.3$ μm, and $\gamma = 0.4$ n N/μm, as consistent with MA data (*blue circles*). Error bars indicate the experimental SD. Guide-lines with BWdG, JKR, and DMT limits are provided as indication. We have assumed $R = 6$ μm. (*b*) Parameter space of E_c, t_c, and γ, with an isosurface obtained from simulations of MA on S180 cells, which delimits all parameter combinations for which the experimentally observed critical pressure $P_c = 250$ Pa (12) is attained. Colored dots represent new samples in this surface for which simulations of DPA were performed. The color scale indicates the value of $\overline{F}_s = F_s/\pi\widehat{R}w$ obtained for an adhesion energy of $w = 0.5$ n N/μm. The overlaid rectangular lattice depicts the grid in which MA simulations were performed. To see this figure in color, go online.

γ. This confirms our hypothesis that either the presence of active tension or a larger "effective thickness" is required to explain the adhesive behavior of cells. Moreover, it can be observed that a manyfold increase of t_c is required to have the same effect as a moderate active tension. Under the assumption that the apparent increase in t_c is moderate, $t_c = 0.3$ μm, we estimate for S180 cells that $\gamma \approx 0.4$ n N/μm and $E_c \approx 15$ kPa. The full parameter set of estimated properties is listed in Table 1. It should be stressed that the goal of this work is not to determine the mechanical properties of S180 cells but rather to demonstrate a quantitative relationship obtained between E_c, t_c, and γ and provide an estimate for the range of possible parameters.

We performed simulations of DPA with the parameters from Table 1 for varying adhesion energy and overlay the resulting $\overline{F}_s$ with experimental values from (7)—see Fig. 4 *a*. A reasonable agreement is found between simulation and experiment, and in both cases, a small decrease of $\overline{F}_s$ with w is observed, with $\overline{F}_s \approx 2$ for small w and $\overline{F}_s \approx 3/2$ for larger w. This trend is similar to the transition observed for solid elastic spheres: w affects the Tabor parameter $\mu = \widehat{R}^{1/3} w^{2/3} \widehat{E}^{-2/3} z_0^{-1}$ (with effective range of interaction $h_0 \approx 0.97 z_0$) (11) that describes the transition between JKR-like and DMT-like adhesion. Although we were not able to formulate a similar universal transition parameter for our more complex modeled system, the underlying mechanisms can be similar: at low w, h_0 is large compared to the contact radius, and the region of adhesive traction is affected little by elastic deformation (DMT assumption). At large w, the elastic deformation is much greater than h_0 and fully determines the adhesive region (JKR assumption).

To further verify the obtained estimates of the mechanical properties of S180 cells, we compare them to a third, separate experimental method. Al-Kilani et al. (25) studied the stiffness of cell-bead contacts for spread S180 cells on adhesive patches of various size using an optical trap. For small patch sizes ($<2R$), the spread cell remains reasonably rounded, and the conditions are comparable to the suspension setting of the MA and DPA experiments. An adhesive bead of diameter 3.6 μm, maintained in an optical trap, was laterally attached to the spread cell. Next, a force F_{app} was applied to the bead by moving the stage in the optical trap. An apparent Young's modulus of the cell was computed as

$$E_{\text{app}} = \frac{3}{4} \frac{F_{\text{app}}}{2 a_c x_c}, \tag{3}$$

with a_c the cell-bead contact radius and x_c the observed bead displacement. For mature adhesion between cell and bead (adhesion time more than 15 min), they obtained $E_{\text{app}} \approx 600 \pm 140$ Pa. Using the estimated mechanical properties of S180 cells (Table 1), we replicated this setup in our model for the smallest patch size $L = 10$ μm—Fig. 5 *a*. The cell-bead adhesion energy was tuned $w_{cb} = 0.517$ nN/μm to match the experimentally observed contact radius $a_c \approx 1.59$ μm—see Fig. 5 *b*, inset. We then measured the ratio $\Delta F_{\text{app}}/\Delta x_c$ for small pulling forces and obtained $E_{\text{app}} \approx 688.4$ Pa using Eq. 3—Fig. 5 *b*. This value is in line with the experimental value for mature adhesions. For immature adhesions, lower values of E_{app} were reported in (25). In their study, this was attributed

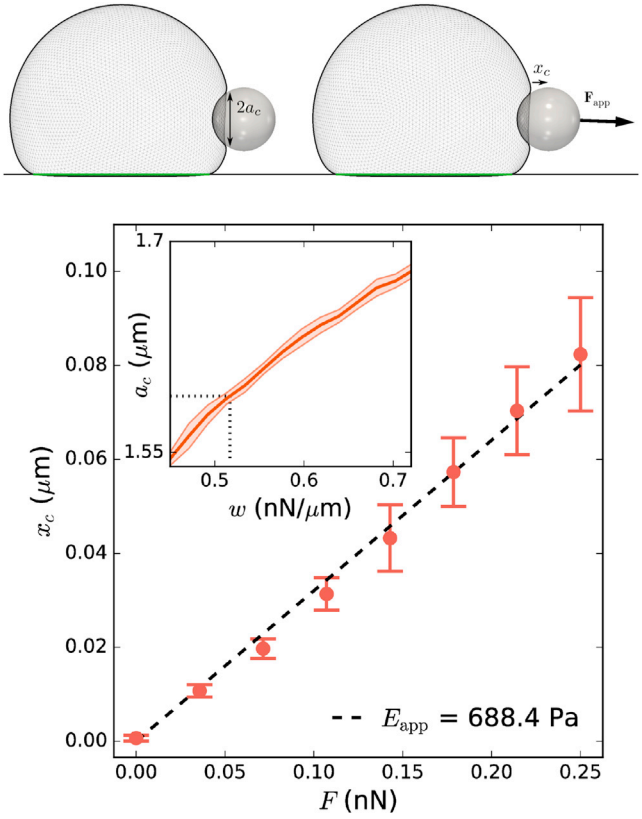

FIGURE 5 Simulation of optical tweezers experiment. Top: a visualization of simulation of optical trap experiment based on (25). A cell is allowed to adhere on a square adhesive pattern (*green*) to obtain a controlled spread size. Then, a spherical adhesive bead adheres to the cell until contact radius a_c is attained (*left*). Next, an external force $\mathbf{F}_{\text{app}}$ is applied to the bead, and its displacement x_c is recorded (*right*). Bottom: apparent Young's modulus computed as $E_{\text{app}} = 3F_{\text{app}}/(8a_c x_c)$ in function of the cell radius for a cell with the estimated mechanical properties of an S180 cell (Table 1). Error bars indicate the SD across independent rotations of the cell. Inset: calibration of cell-bead adhesion energy $w_{cb} = 0.517$ nN/μm using the contact radius a_c . The dotted line indicates the experimentally observed contact radius. The shaded region indicates the SD across independent rotations of the cell. To see this figure in color, go online.

TABLE 1 Table of Numerically Estimated Mechanical Properties of S180 Cells That Is Consistent with MA and DPA Experiments

Parameter	Symbol	Value	Unit	Derived from
Cortex stiffness	E_c	15	kPa	MA + DPA (7,12)
Poisson's ratio cortex	ν_c	1/3	–	assumed
Thickness cortex	t_c	0.3	μm	(16,19–21), Fig. 4
Active tension	γ	0.4	nN/μm	MA + DPA (7,12)
Bulk modulus cell	K	30	kPa	assumed, Fig. S7
Cell radius	R	6	μm	(7,25,36)
Adhesive range	h_0	50	nm	(24)

to the lowered rigidity of the still-immature adhesion complexes themselves, which unravel upon application of tensile force. Because we considered the contacts nearly rigid ($E_c \gg E_{app}$), our estimated apparent stiffness could be considered an upper limit of the combined cytoskeleton-adhesion complex system.

Contact radius

For the parameters in Table 1 and $w = 0.6$ nN/μm (hence, $\kappa \approx 0.87$), we investigate in detail the change of contact radius R_c with increase of the applied pulling force F in a DPA experiment. For solid elastic spheres, the contact radius depends on the elastic modulus $\widehat{E}_{cell}$. For DMT and JKR, the cube of the contact radius is given by

$$R^3_{c,DMT} = \frac{3\widehat{R}}{4\widehat{E}_{cell}}\left(2\pi\widehat{R}w - F\right), \tag{4}$$

$$R^3_{c,JKR} = \frac{3\widehat{R}}{4\widehat{E}_{cell}}\left(3\pi\widehat{R}w + \sqrt{-6\pi\widehat{R}wF + \left(3\pi\widehat{R}w\right)^2} - F\right). \tag{5}$$

Further, we will define the relative contact radius $\psi := R_c/R$. For the BWdG model for adhesive vesicles with surface tension, the relationship between applied pull force and contact radius is nontrivial and is expressed in function of the deformed apex radius R_a (8) with $\psi' := R_c/R_a$:

$$F = \frac{\pi R_a \psi'}{1-\psi'^2}\left(\sqrt{w(4\gamma - w)} - 2\gamma\psi'\right). \tag{6}$$

Fig. 6 shows ψ and ψ' as a function of F for a simulated cell, compared to the theoretical predictions of DMT, JKR, and BWdG. For DMT and JKR, we expect the change of apical radius to be small, so approximate $R_a \approx R$, hence $\psi' \approx \psi$. From this comparison, we list the following observations:

1) Pull-off force is close to the JKR limit. The maximal contact radius at $R = 0$ corresponds to an apparent elastic modulus—obtained from Eq. 5—$\widehat{E}_{cell} \approx 600$ Pa. However, the change of contact radius with force does not follow JKR theory. The dependency of the effective $\widehat{E}_{cell}$ on γ is further shown in Fig. S4.
2) Rupture occurs at much higher tensile loading than for ideal adhesive vesicles with surface tension (BWdG) because of the presence of bending resistance, which ensures the maintenance of low contact angles. The maximal contact radius at $F = 0$ corresponds to an adhesive vesicle with a surface tension of $\sim$0.8 nN/μm, which is in close agreement with the value of 0.9 nN/μm obtained from the analysis of the MA experiment, assuming that the cell is a liquid droplet with surface tension (12). This correspondence of cell contact radius to the BWdG model in (self- or externally) compressed conditions but not during tensile loading and pull-out has been observed experimentally on HeLa cells in (26).
3) At low F (large contacts), the change of ψ with F is DMT-like, i.e., $d_\psi F \approx -32\,\widehat{E}_{cell}\,\widehat{R}^2\,\psi^2$, with an apparent $\widehat{E}_{cell} \approx 200$ Pa when using Eq. 4. This indicates that the force-indentation $F(\delta)$ response of adherent cells with surface tension is remarkably Hertzian. This observation was confirmed in a simulated compression test on a spread-out cell: around $F = 0$, the contact force follows $F \sim \delta^{3/2}$ (see Fig. S5). This contrasts with the force-deformation response of a liquid-filled shell with no adhesion or active tension, which showcases cubic behavior $F \sim \delta^3$ (27).

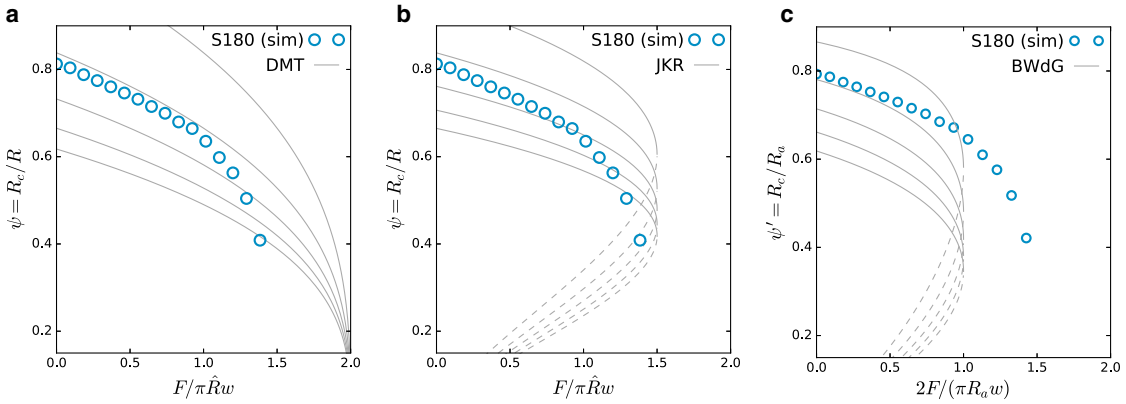

FIGURE 6 Normalized contact radii ψ and ψ' as a function of normalized applied force $F/\pi\widehat{R}w$ of a simulated S180 DPA pull-off experiment (parameters in Table 1) and for $w = 0.6$ nN/μm, compared to (*a*) DMT, (*b*) JKR, and (*c*) BWdG limits. For solid elastic spheres (JKR and DMT), we assume that $R_a \approx R$. Dashed lines indicate where contact is not stable and rupture of the cell doublet will occur. Different guide lines are shown (from *top* to *bottom* at $F = 0$) for DMT: $\widehat{E}_{cell}$ (Pa) $\in \{100, 200, 300, 400, 500\}$; for JKR: $\widehat{E}_{cell}$ (Pa) $\in \{400, 600, 800, 1000, 1200\}$; and for BWdG: γ (nN/μm) $\in \{0.6, 0.8, 1.0, 1.2, 1.4\}$. To see this figure in color, go online.

DISCUSSION

In this work, we have quantified the adhesion behavior of filled elastic shells with active tension, which were used as a model for biological cells. Numerical simulations with this model were carried out to investigate the role of cortical stiffness, thickness, and active tension. These simulations showed that a combination of these properties can simultaneously explain the mechanics of cell deformation during aspiration and of cell-cell separation during a pull-off experiment. We estimate that cells exist in small to moderate ranges of a dimensionless thickness κ. In these conditions, the active tension plays a crucial role, and is required to explain the observed scaling of separation force.

Cortex mechanics

By comparison to existing experiments on S180 cells, we give tentative estimates of mechanical properties of their actin cortex that agree with characterizations in literature (7,12,16,25). In contrast to a solid elastic model, a model of adhesive, tensed elastic shells can provide consistent estimates of mechanical properties across different mechanical experiments. We estimated an active tension of 0.4 nN/μm, in good agreement with other measurements of active tension, e.g., 0.41 nN/μm on L929 fibroblasts (13), 0.3 nN/μm on chick embryo fibroblasts (28), and 0.2 nN/μm on HeLa cells (29). Measurements of cortical stiffness in literature vary greatly, ranging from 1 kPa (5) to 40 kPa (16,30), encompassing our estimate of 15 kPa. Of note is the over sixfold lower value of 2.4 kPa obtained on L929 cells, even though it was derived using a similar mechanical description of the cell (13). Aside from obvious differences in cell type, this discrepancy could be attributed to various explanations. First, they also include elastic deformation of the cytosol, whereas we have lumped any such effect in an "effective" increase of cortex thickness. Secondly, any loss of contractility near the bleb induced by laser ablation might have significantly reduced the apparent stiffness of the actin cortex that exhibits stress stiffening properties (31). An active tension of 0.4 nN/μm corresponds to a contractile stress of $>$1 kPa. For such a stress, the apparent stiffness of a cross-linked actin network is $>$1000 times higher than the stiffness in stress-free conditions (18). For simplicity, we have set Poisson's ratio of the cortex to $\nu_c = 1/3$. In (13), a value of 1/2 was assumed. In biomimetic actin networks, Poisson's ratio was estimated at $\nu_c = 0.1$ (32). Because its main contribution is through a factor of $(1 - \nu_c^2)$ in the bending rigidity (see Supporting Materials and Methods), we expect ν_c to be of relatively minor importance.

Force-deformation behavior

We show that JKR-like pull-off forces can exist for a wide range of adhesion energies. Furthermore, the scaling of contact radius with force at low loading force (or, conversely, large adhesive deformation) follows BWdG predictions but is also consistent with DMT theory, implying that force-deformation behavior is Hertz-like at sufficient deformation. This suggests that in an indentation experiment, for example, atomic force microscopy, this model would be almost indistinguishable from a solid elastic material. Because Hertz theory is ubiquitously used in atomic force microscopy experiments to parameterize cells with an apparent Young's modulus, this begs the question of when its application is appropriate and when not. It can be argued that for strongly spread-out cells, where dense cytoskeletal material spans the full height of the cell, this parameterization is apt. Our results indicate that for cells that are more rounded in shape, e.g., suspension cells (7), weakly adhering cells (16,25), or cells in dense packings (5), the description of a cell as a tensed shell is more consistent across experimental methods and conditions.

Limitations

We have presented a minimalistic mechanical model that disregards most of the complexities that accompany cell-cell adhesion in real biological settings. Some of these complications can well be expected to affect the results presented here in a nontrivial manner, and they will be briefly discussed.

Firstly, we considered the cell's cytosol as liquid-like (i.e., bearing hydrostatic stresses, and this through an effective bulk modulus K). The physical properties of the cell's internal structures are complex, and models that capture its mechanical behavior are often dependent on the timescale of interest. At fast timescales ($\ll$10 s), indented cells show a viscoelastic creep response, which might be attributed to Maxwell fluid behavior of the cell's internal structures (33). The contribution of the cytosol's elasticity was shown to be important for controlling the (fast) growth of blebs (13). The assumption in our analyses was that experiments were at least slow enough to relax any deviatoric stresses in the cytosol.

Secondly, our shell model consists of linearly elastic material, whereas the cell cortex has been shown to exhibit nonlinear behavior at large deformations, including both strain stiffening and strain softening (17). Typical strains in our simulated experiments are very low ($<$5%) but can locally reach up to 20%, e.g., near rupture at the contact site in a pull-off experiment. Here, nonlinearities in stretch response could have non-negligible effect on the separation force.

Finally, we model adhesion based on the assumption of fixed and nonspecific stickers (or with a mobility timescale that is much slower than the timescale of bond rupture). This assumption is valid for the experiment we compared our results against, in which depletion-induced adhesion was studied. In naturally adhering cells, adhesive ligands have been shown to diffuse in the plasma membrane and cluster

at the site of cell-cell junctions (34). All these phenomena are expected to affect adhesion and debonding mechanics, both dynamically and at steady state (35). Although not the focus of this study, these properties need to be taken into account to model cell-cell adhesion in realistic biological settings.

SUPPORTING MATERIAL

Supporting Materials and Methods, nine figures, and five tables are available at http://www.biophysj.org/biophysj/supplemental/S0006-3495(19)30050-5.

AUTHOR CONTRIBUTIONS

B.S. designed research. B.S. and J.P. performed research. B.S., J.P., M.C., and H.R. wrote the manuscript.

ACKNOWLEDGMENTS

We thank S. Vanmaercke for technical support in designing the computational algorithms for the numerical simulations.

We acknowledge the interdisciplinary research funding of KU Leuven (IDO/13/016) for financial support. B.S. acknowledges support from the Research Foundation-Flanders, Grant Nr. 12Z6118N.

REFERENCES

1. Desprat, N., A. Richert, …, A. Asnacios. 2005. Creep function of a single living cell. *Biophys. J.* 88:2224–2233.
2. Kollmannsberger, P., and B. Fabry. 2009. Active soft glassy rheology of adherent cells. *Soft Matter.* 5:1771–1774.
3. Lim, C. T., E. H. Zhou, and S. T. Quek. 2006. Mechanical models for living cells–a review. *J. Biomech.* 39:195–216.
4. Hochmuth, R. M. 2000. Micropipette aspiration of living cells. *J. Biomech.* 33:15–22.
5. Maître, J. L., H. Berthoumieux, …, C. P. Heisenberg. 2012. Adhesion functions in cell sorting by mechanically coupling the cortices of adhering cells. *Science.* 338:253–256.
6. Kuznetsova, T. G., M. N. Starodubtseva, …, R. I. Zhdanov. 2007. Atomic force microscopy probing of cell elasticity. *Micron.* 38:824–833.
7. Chu, Y. S., S. Dufour, …, F. Pincet. 2005. Johnson-Kendall-Roberts theory applied to living cells. *Phys. Rev. Lett.* 94:028102.
8. Brochard-Wyart, F., and P. G. de Gennes. 2003. Unbinding of adhesive vesicles. *C. R. Phys.* 4:281–287.
9. Johnson, K. L., K. Kendall, and A. D. Roberts. 1971. Surface energy and the contact of elastic solids. *Proc. R. Soc. Lond. A Math. Phys. Sci.* 324:301–313.
10. Derjaguin, B. V., V. M. Muller, and Y. P. Toporov. 1975. Effect of contact deformations on the adhesion of particles. *J. Colloid Interface Sci.* 53:314–326.
11. Johnson, K. L., and J. A. Greenwood. 1997. An adhesion map for the contact of elastic spheres. *J. Colloid Interface Sci.* 192:326–333.
12. Engl, W., B. Arasi, …, V. Viasnoff. 2014. Actin dynamics modulate mechanosensitive immobilization of E-cadherin at adherens junctions. *Nat. Cell Biol.* 16:587–594.
13. Tinevez, J. Y., U. Schulze, …, E. Paluch. 2009. Role of cortical tension in bleb growth. *Proc. Natl. Acad. Sci. USA.* 106:18581–18586.
14. Fischer-Friedrich, E., Y. Toyoda, …, F. Jülicher. 2016. Rheology of the active cell cortex in mitosis. *Biophys. J.* 111:589–600.
15. Shi, J., S. Muftu, and K.-T. Wan. 2011. Adhesion of an elastic convex shell onto a rigid plate. *J. Adhes.* 87:579–594.
16. Cartagena-Rivera, A. X., J. S. Logue, …, R. S. Chadwick. 2016. Actomyosin cortical mechanical properties in nonadherent cells determined by atomic force microscopy. *Biophys. J.* 110:2528–2539.
17. Kubitischke, H., J. Schnauss, …, J. Kaes. 2017. Actin and microtubule networks contribute differently to cell response for small and large strains. *New J. Phys.* 19:093003.
18. Gardel, M. L., F. Nakamura, …, D. A. Weitz. 2006. Prestressed F-actin networks cross-linked by hinged filamins replicate mechanical properties of cells. *Proc. Natl. Acad. Sci. USA.* 103:1762–1767.
19. Charras, G. T., C. K. Hu, …, T. J. Mitchison. 2006. Reassembly of contractile actin cortex in cell blebs. *J. Cell Biol.* 175:477–490.
20. Clark, A. G., K. Dierkes, and E. K. Paluch. 2013. Monitoring actin cortex thickness in live cells. *Biophys. J.* 105:570–580.
21. Cuvelier, D., M. Théry, …, L. Mahadevan. 2007. The universal dynamics of cell spreading. *Curr. Biol.* 17:694–699.
22. Odenthal, T., B. Smeets, …, H. Ramon. 2013. Analysis of initial cell spreading using mechanistic contact formulations for a deformable cell model. *PLoS Comput. Biol.* 9:e1003267.
23. Kot, M., H. Nagahashi, and P. Szymczak. 2015. Elastic moduli of simple mass spring models. *Vis. Comput.* 31:1339–1350.
24. Israelachvili, J. N. 2011. Intermolecular and Surface Forces, Third Edition. Academic Press, London, UK.
25. Al-Kilani, A., O. de Freitas, …, F. Gallet. 2011. Negative feedback from integrins to cadherins: a micromechanical study. *Biophys. J.* 101:336–344.
26. Colbert, M. J., F. Brochard-Wyart, …, K. Dalnoki-Veress. 2010. Squeezing and detachment of living cells. *Biophys. J.* 99:3555–3562.
27. Lulevich, V. V., D. Andrienko, and O. I. Vinogradova. 2004. Elasticity of polyelectrolyte multilayer microcapsules. *J. Chem. Phys.* 120:3822–3826.
28. Thoumine, O., O. Cardoso, and J. J. Meister. 1999. Changes in the mechanical properties of fibroblasts during spreading: a micromanipulation study. *Eur. Biophys. J.* 28:222–234.
29. Fischer-Friedrich, E., A. A. Hyman, …, J. Helenius. 2014. Quantification of surface tension and internal pressure generated by single mitotic cells. *Sci. Rep.* 4:6213.
30. Bausch, A. R., F. Ziemann, …, E. Sackmann. 1998. Local measurements of viscoelastic parameters of adherent cell surfaces by magnetic bead microrheometry. *Biophys. J.* 75:2038–2049.
31. Gardel, M. L., J. H. Shin, …, D. A. Weitz. 2004. Elastic behavior of cross-linked and bundled actin networks. *Science.* 304:1301–1305.
32. Bussonnier, M., K. Carvalho, …, T. Betz. 2014. Mechanical detection of a long-range actin network emanating from a biomimetic cortex. *Biophys. J.* 107:854–862.
33. Yango, A., J. Schäpe, …, M. Radmacher. 2016. Measuring the viscoelastic creep of soft samples by step response AFM. *Soft Matter.* 12:8297–8306.
34. Sackmann, E., and A. S. Smith. 2014. Physics of cell adhesion: some lessons from cell-mimetic systems. *Soft Matter.* 10:1644–1659.
35. de Gennes, P.-G., P.-H. Puech, and F. Brochard-Wyart. 2003. Adhesion induced by mobile stickers: a list of scenarios. *Langmuir.* 19:7112–7119.
36. Chu, Y. S., W. A. Thomas, …, S. Dufour. 2004. Force measurements in E-cadherin-mediated cell doublets reveal rapid adhesion strengthened by actin cytoskeleton remodeling through Rac and Cdc42. *J. Cell Biol.* 167:1183–1194.

Biophysical Journal, Volume *116*

Supplemental Information

The Effect of Cortical Elasticity and Active Tension on Cell Adhesion Mechanics

Bart Smeets, Maxim Cuvelier, Jiri Pešek, and Herman Ramon

The effect of cortical elasticity and active tension on cell adhesion mechanics
Supplementary Information

B. Smeets, M. Cuvelier, J. Pešek, H. Ramon

KU Leuven – MeBioS, Kasteelpark Arenberg 30, 3001 Heverlee, Belgium

1 Computational Method

Contact Mechanics In our numerical model, we represent deformable cells as triangulated meshes, where the local curvature is taken into account for each triangle by means of an encompassing sphere. The contact between two rounded triangles can be modeled by using the Maugis-Dugdale (MD) theory for overlapping spheres (1).

MD expands upon Hertz' pure repulsive contact model by taking into account the adhesive pressure associated with intimate contact between adherent surfaces – see Fig. S1. The MD contact pressure between two curved asperities A and B is given by the sum of Hertz and adhesive pressures:

$$p(r) = p_a(r) + p_H(r). \tag{S1}$$

The repulsive Hertz pressure acting on the contact area with radius a, for a given distance r from the center of the contact circle, is given by

$$p_H(r) = \frac{2\hat{E}_{AB}}{\pi \hat{R}_{AB}} \sqrt{a^2 - r^2}, \tag{S2}$$

with effective Young's modulus $\hat{E}_{AB}$ and contact radius $\hat{R}_{AB}$

$$\hat{E}_{AB} = \left(\frac{1-\nu_A^2}{E_A} + \frac{1-\nu_B^2}{E_B} \right)^{-1},$$

$$\hat{R}_{AB} = \left(\kappa_A + \kappa_B \right)^{-1},$$

where E_A, ν_A and κ_A refer to the Young's modulus, Poisson ratio and local curvature of a given asperity A. Adhesive stress is given by

$$p_a(r) = \begin{cases} -\frac{\sigma_0}{\pi} \arccos\left(\frac{2a^2 - c^2 - r^2}{c^2 - r^2} \right) & 0 < r < a, \\ -\sigma_0, & a < r < c, \end{cases} \tag{S3}$$

Here, σ_0 represents the maximal adhesive traction, which is related to the adhesion energy w as (3):

$$w = h_0 \, \sigma_0, \tag{S4}$$

where h_0 represents the maximum separation between the asperities beyond which the adhesive traction drops to zero.

Numerical integration of the contact pressures allows us to determine the net contact force and moment acting on a pair of triangles $(\alpha\beta)$. Assuming that the nodal contact forces $F_i^{\alpha\beta}$ must be colinear with the contact unit normal $\hat{\boldsymbol{n}}_{\alpha\beta}$, the system of linear equations per contact pair $(\alpha\beta)$:

$$\sum_{i \in \alpha} \boldsymbol{F}_i^{\alpha\beta} = - \sum_{q \in \alpha \cap \beta} A_q \, p(\|\boldsymbol{r}_q\|) \hat{\boldsymbol{n}}_{\alpha\beta}, \tag{S5}$$

$$\sum_{i \in \alpha} \left[\boldsymbol{x}_i - \boldsymbol{x}_C^{\alpha\beta} + \left[(\boldsymbol{x}_C^{\alpha\beta} - \boldsymbol{x}_i) \cdot \hat{\boldsymbol{n}}_{\alpha\beta} \right] \hat{\boldsymbol{n}}_{\alpha\beta} \right] \times \boldsymbol{F}_i^{\alpha\beta} = - \sum_{q \in \alpha \cap \beta} A_q p(\|\boldsymbol{r}_q\|) \boldsymbol{r}_q \times \hat{\boldsymbol{n}}_{\alpha\beta}, \tag{S6}$$

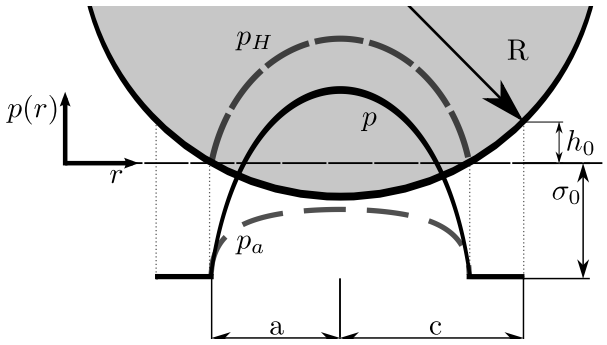

Figure S1: Illustration of contact between an asperity with radius R and a flat half-space. The total contact pressure p is the sum of the repulsive Hertz pressure p_H, acting within contact radius a and an adhesive Dugdale traction p_a, acting within contact radius c. For $a \leq r \leq c$, the adhesive traction is at its maximal value σ_0.

results in a unique solution for every $\boldsymbol{F}_i^{\alpha\beta}$. A_q is the weighted area associated with quadrature points q, covering the intersection polygon $\alpha \cap \beta$. $\boldsymbol{r}_q$ is the vector from the sphere-sphere[1] contact point $\boldsymbol{x}_C^{\alpha\beta}$ to the quadrature point. The solution for this system is presented in Odenthal et al. (1).

Cortex Elasticity Assuming small deformations, we use the Van Gelder model to approximate in-plane elastic behavior of the cortex using linear springs (4):

$$\boldsymbol{F}_{ij}^s = k_s(d_{ij} - d_{ij}^*)\hat{\boldsymbol{n}}_{ij}, \tag{S7}$$

with

$$\hat{\boldsymbol{n}}_{ij} = \frac{\boldsymbol{x}_j - \boldsymbol{x}_i}{\|\boldsymbol{x}_j - \boldsymbol{x}_i\|}, .$$

Here, $d_{ij} = \|\boldsymbol{x}_j - \boldsymbol{x}_i\|$ is the current distance and d_{ij}^* the resting distance between nodes i and j with positions $\boldsymbol{x}_i$ and $\boldsymbol{x}_j$. The linear spring stiffness k_s, under our assumption of an isotropic linear elastic material model, can be expressed as a function of E_c and t_c using Van Gelder's formula (4):

$$k_s = \frac{E_c t_c \left(A_{ij}^{\alpha} + A_{ij}^{\beta}\right)}{{d_{ij}^*}^2}, \tag{S8}$$

in which $A_{ij}^{\alpha} + A_{ij}^{\beta}$ is the area of the connected triangle pair $\alpha\beta$ – see Fig. S2(a). By using this expression we have implicitly assumed that the Poisson ratio is equal to $1/3$ (6). Due to its non-zero thickness, the cortex also has bending rigidity. The energy required to bend two connected triangles $(\alpha\beta)$ is given by

$$E_{\alpha\beta}^b = k_b\left(1 - \cos\left(\theta - \theta^*\right)\right), \tag{S9}$$

where θ^* and θ represent the spontaneous and instantaneous angles between a pair of adjacent triangles.

As with k_s, bending rigidity k_b can be estimated based on cortex properties to match to macroscopic (continuum) models. Based on the model of Helfrich (5)

$$k_b = \frac{E_c t_c^3}{12\left(1 - \nu_c^2\right)}, \tag{S10}$$

with ν_c Poisson's ratio of the cortex. To be consistent with the assumption of an isotropic linear elastic material, ν_c is fixed at a value of $1/3$ (6), hence $k_b = 3E_c\, t_c^3/32$. For a pair of connected triangles $\alpha\beta$, the bending moment is:

$$\boldsymbol{M}_{\alpha\beta}^b = -k_b(\theta - \theta^*)\frac{\boldsymbol{x}_{\alpha\beta}^{c2} - \boldsymbol{x}_{\alpha\beta}^{c1}}{\left\|\boldsymbol{x}_{\alpha\beta}^{c2} - \boldsymbol{x}_{\alpha\beta}^{c1}\right\|}, \tag{S11}$$

for small angle deviations when $\sin\left(\theta - \theta^*\right) \approx \theta - \theta^*$, and with $\boldsymbol{x}_{\alpha\beta}^{c1}$ and $\boldsymbol{x}_{\alpha\beta}^{c2}$ the positions of the connected triangles' common nodes, sorted counter-clockwise with respect to the triangle normal vectors $\hat{\boldsymbol{n}}_\alpha$ and $\hat{\boldsymbol{n}}_\beta$ – see Fig. S2(b). This couple

[1] Each triangle with curvature κ can be associated with a unique sphere with radius $1/\kappa$, see (1).

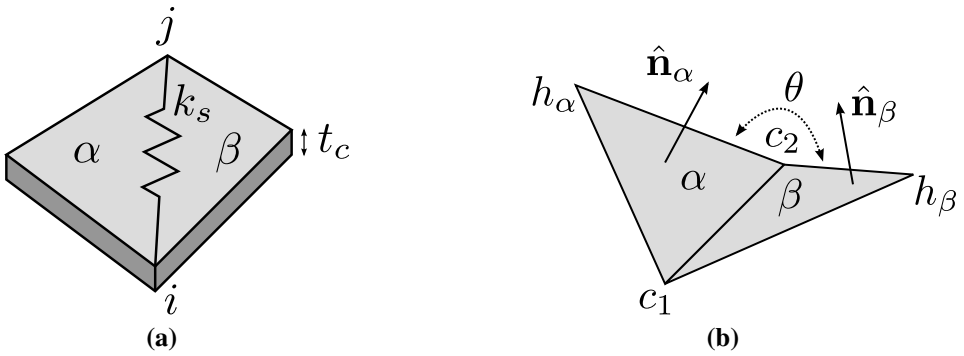

Figure S2: **(a)**: Illustration of elementary spring element between nodes i and j. The spring constant k_s is based on a thin shell element containing adjacent triangles α and β, and with thickness t_c – Eq. (S8). **(b)**: Illustration of two connected triangles α and β with normal unit vectors $\hat{\boldsymbol{n}}_\alpha$ and $\hat{\boldsymbol{n}}_\beta$ between whom a bending moment is computed based on the instantaneous angle θ. Furthermore, we have indicated (sorted) common nodes c_1 and c_2 and lever nodes h_α and h_β.

is translated to mechanically equivalent forces on the four nodes of the triangle pair. For each triangle, the sum of all three forces must be zero, and the generated moment w.r.t. the common axis must be $\boldsymbol{M}^b_{\alpha\beta}$. These conditions lead to following unique total nodal forces:

$$\boldsymbol{F}^{h_\alpha}_{\alpha\beta} = -\boldsymbol{M}^b_{\alpha\beta} \times \boldsymbol{h}_\alpha, \tag{S12}$$

$$\boldsymbol{F}^{h_\beta}_{\alpha\beta} = \boldsymbol{M}^b_{\alpha\beta} \times \boldsymbol{h}_\beta, \tag{S13}$$

$$\boldsymbol{F}^{c1}_{\alpha\beta} = \frac{y^{c2}_\beta}{y^{c1}_\beta - y^{c2}_\beta}\left(\boldsymbol{M}^b_{\alpha\beta} \times \boldsymbol{h}_\beta\right) - \frac{y^{c2}_\alpha}{y^{c1}_\alpha - y^{c2}_\alpha}\left(\boldsymbol{M}^b_{\alpha\beta} \times \boldsymbol{h}_\alpha\right), \tag{S14}$$

$$\boldsymbol{F}^{c2}_{\alpha\beta} = \frac{y^{c1}_\beta}{y^{c2}_\beta - y^{c1}_\beta}\left(\boldsymbol{M}^b_{\alpha\beta} \times \boldsymbol{h}_\beta\right) - \frac{y^{c1}_\alpha}{y^{c2}_\alpha - y^{c1}_\alpha}\left(\boldsymbol{M}^b_{\alpha\beta} \times \boldsymbol{h}_\alpha\right). \tag{S15}$$

h_α and h_β indicate the indices of the (non-common) "lever" node of triangles α and β. $\boldsymbol{h}_\alpha$ and $\boldsymbol{h}_\beta$ are the orthogonal height vectors from the common axis to lever nodes h_α and h_β. Finally,

$$y^{cj}_k = (\boldsymbol{x}^{cj}_{\alpha\beta} - \boldsymbol{x}^{h_k}_{\alpha\beta}) \cdot (\boldsymbol{x}^{c2}_{\alpha\beta} - \boldsymbol{x}^{c1}_{\alpha\beta}), \tag{S16}$$

for $k \in [\alpha, \beta]$ and $j \in [1, 2]$.

Active cortical tension Tension generated in the cortex results form myosin contractility which can be be interpreted as an effective surface tension γ in the cortical shell model. γ helps in maintaining cell shape and decreases the local curvature on longer time-scales. Based on the Young-Laplace law, the pressure contribution due to γ is given by

$$P^\gamma_i = -2\gamma\kappa_i, \tag{S17}$$

with κ_i being the local curvature. Active volume control also contributes to the cytoplasmic pressure. As the equilibrium volume of a cell is assumed to be constant at short time-scales, an effective bulk modulus K is introduced. The cytoplasmic pressure due to volume control P^v can thus be estimated as

$$P^v = -K\frac{V - V^*}{V^*}. \tag{S18}$$

V^* and V represent the spontaneous and instantaneous volume of the cell. The resulting nodal force due to the total internal pressure P is given by

$$\boldsymbol{F}^p_i = \hat{\boldsymbol{n}}_i \mathcal{A}_i P_i = \hat{\boldsymbol{n}}_i \mathcal{A}_i \left(P^\gamma_i + P^o + P^v\right), \tag{S19}$$

with $\mathcal{A}_i$ and $\hat{\boldsymbol{n}}_i$ the Voronoi area (1) and normal associated with a given node. Moreover, we assume that a constant (e.g. osmotic) pressure $P^o = 2\gamma/R$ exists that ensures that the free cell is mechanically at rest.

Dissipative forces Our method is based on solving overdamped equations of motion. Hence, dissipative forces are required to balance these equations of motion. The general methodology tries to introduce these dissipative forces in a consistent manner in terms of viscosities of modeled materials. A general drag force $\boldsymbol{F}_i^l$ is included to account for the liquid drag between the cells and their medium:

$$\boldsymbol{F}_i^l = -\lambda_l \mathcal{A}_i \boldsymbol{v}_i, \tag{S20}$$

with $\mathcal{A}_i$ the Voronoi area of node i. For spherical cells with radius R

$$\lambda_l = \frac{3\eta_l}{2R} \tag{S21}$$

can be used to estimate λ_l, introducing fluid viscosity η_l. When dealing with arbitrary shapes this approximation is no longer correct and we would in principle require the microscopic resolution of the fluid flow field in and around the cell surface. However, as F_i^d is typically very small compared to other dissipative forces at the seconds/minutes timescale, this approximation is sufficient. Likewise, we can increase the fluid viscosity above realistic values to dampen numerical oscillations without any influence on simulation results. A much larger contribution to energy dissipation arises from viscosity of the cortex itself. The viscous damping force between two connected nodes i and j is computed as

$$\boldsymbol{F}_{ij}^d = \Lambda_{ij}^d (\boldsymbol{v}_j - \boldsymbol{v}_i), \tag{S22}$$

with friction elements ($\boldsymbol{I}$ being identity)

$$\Lambda_{ij}^d = \frac{t_c\, \eta_c}{\sqrt{3}}\, \boldsymbol{I}.$$

where the $1/\sqrt{3}$ factor accounts for the triangular connectivity of the shell. Finally, a viscous contact force is included to account for drag between contacting triangles. The contact drag force acting on node i of triangle α of the contacting pair $(\alpha\beta)$

$$\boldsymbol{F}_{\alpha\beta,i}^c = \Lambda_{\alpha\beta}^c \cdot \sum_{\forall k \in \beta} w_{\alpha\beta,ik}\, (\boldsymbol{v}_k - \boldsymbol{v}_i), \tag{S23}$$

again, determined by a friction tensor $\Lambda_{\alpha\beta}^c$ and weights $w_{\alpha\beta,ik}$ per node k of the β triangle. $w_{\alpha\beta,ik}$ are assumed to scale with the relative contribution of the nodal contact forces to the overall contact force, thus

$$w_{\alpha\beta,ik} = \frac{(\boldsymbol{F}_{\alpha\beta,i} + \boldsymbol{F}_{\alpha\beta,k}) \cdot \hat{\boldsymbol{n}}_{\alpha\beta}}{6 \sum\limits_{\forall k \in \beta} \boldsymbol{F}_{\alpha\beta,k}^{MD} \cdot \hat{\boldsymbol{n}}_{\alpha\beta}}, \tag{S24}$$

$\Lambda_{\alpha\beta}^c$ for a given contact area $A_{\alpha\beta}^c$ between triangles α and β is estimated as:

$$\Lambda_{\alpha\beta}^c = A_{\alpha\beta}^c \left[\lambda_n \hat{\boldsymbol{n}}_{\alpha\beta} \cdot \hat{\boldsymbol{n}}_{\alpha\beta}^T + \lambda_t \left(\boldsymbol{I} - \hat{\boldsymbol{n}}_{\alpha\beta} \cdot \hat{\boldsymbol{n}}_{\alpha\beta}^T \right) \right], \tag{S25}$$

with normal and tangential friction coefficients[2] λ_n and λ_t.

Equation of motion Neglecting inertial contributions for the overdamped cellular system, the complete force balance for node i can be expressed based on the different contributions described above

$$\begin{aligned} &\sum_{\text{con.}j} \boldsymbol{F}_{ij}^s + \sum_{(\alpha\beta):i\in\alpha} \boldsymbol{F}_i^{\alpha\beta} + \sum_{(\alpha\beta):i\in\alpha} \boldsymbol{F}_{\alpha\beta,i}^b + \boldsymbol{F}_i^p \\ &= \\ &\sum_{\text{con.}j} \Lambda_{ij}^d \cdot w_{ij}\, (\boldsymbol{v}_i - \boldsymbol{v}_j) + \sum_{(\alpha\beta):i\in\alpha} \left[\Lambda_{\alpha\beta,i}^c \cdot \sum_{\forall k \in \beta} w_{\alpha\beta,ik}\, (\boldsymbol{v}_i - \boldsymbol{v}_k) \right] + \lambda^l \mathcal{A}_i \boldsymbol{v}_i, \end{aligned} \tag{S26}$$

For a system of N nodes, Eq. (S26) can be summarized as:

$$\underline{\boldsymbol{F}} = \underline{\Lambda} \cdot \underline{\boldsymbol{v}}, \tag{S27}$$

[2]Note that the units of friction coefficient λ_n and λ_t are Pa·s/m, as they relate a velocity difference between two contacting surface to a dissipative contact stress.

which consist of a $(3N \times 1)$, $(3N \times 3N)$ and $(3N \times 1)$ matrix for three-dimensional systems. $\underline{\Lambda}$ is a symmetric and positive definite matrix

$$\underline{\Lambda} = \sum_{i,j \in N} \begin{pmatrix} 0 & \cdots & & & \\ \cdots & \Lambda_{ij} & \cdots & -\Lambda_{ij} & \cdots \\ \vdots & \vdots & \ddots & \vdots & \\ \cdots & -\Lambda_{ij} & \cdots & \Lambda_{ij} & \cdots \\ & & & \cdots & 0 \end{pmatrix} + \begin{pmatrix} \lambda_l & 0 & \cdots & & \\ 0 & \lambda_l & 0 & \cdots & \\ \vdots & & \ddots & & \vdots \\ & & 0 & \lambda_l & 0 \\ 0 & & \cdots & 0 & \lambda_l \end{pmatrix}, \tag{S28}$$

where Λ_{ij} are (3×3) matrices created by $w_{ij}\Lambda^d_{ij} + w_{\alpha\beta,ij}\Lambda^c_{\alpha\beta_i}$. Since $\underline{\Lambda}$ is extremely sparse and always positive definite (1, 9), the conjugate gradient method can be used to efficiently solve the system for nodal velocities $\underline{\boldsymbol{v}}(t)$ at each time increment. The positions of the nodes $\underline{\boldsymbol{x}}$ are subsequently updated using a forward Euler scheme:

$$\underline{\boldsymbol{x}}(t + \Delta t) = \underline{\boldsymbol{x}}(t) + \Delta t\, \underline{\boldsymbol{v}}(t). \tag{S29}$$

Implementation The computational model was implemented in the C++ particle-based simulation framework '*Mpacts*'. The deformable cell model was first introduced in (1), and later expaned upon for shell mechanics in (2). For solving over-damped systems, we use a semi-implicit method – see Eq. (S27), where a friction matrix is assembled that contains contact friction (or stiffness) elements. Each timestep, this linear system is iteratively solved using the Conjugate Gradient implementation of the C++ linear algebra library Eigen (10) which is optimized for vectorization and performance. Furthermore, a multi-grid contact detection scheme (11) was used to efficiently resolve pairs of contacting triangles between the contact pressures described above were numerically integrated. Numerical integration was performed using a 7-point symmetric Gaussian quadrature rule as derived in (12). Highly regular triangulated surface meshes of spherical cells were obtained by the progressive subdivision of an icosahedron – see e.g. (1). We used 5-level subdivisions (resulting in 2562 vertices and 5120 triangles) for the results in Fig. 3 and Fig. 4 and 6-level subdivisions (resulting in 10242 vertices and 20480 triangles) for the results in Fig. 6, where a greater refinement was adopted for the estimates of contact radius.

2 Simulation setup

Here, we summarize the technical aspects of the performed simulations. In this work, we have considered four distinct setups: MA, DPA, optical tweezers and, very briefly, compression between two parallel plates.

Table S1: Complete list of parameters used to simulate the MA experiments shown in Fig. 4(b). Square brackets indicate ranges of parameters that were varied across multiple simulations.

Parameter	**Symbol**	**Value(s)**	**Units**
Young's modulus cortex	E_c	[5, 35]	kPa
Poisson's ratio cortex	ν_c	1/3	-
Thickness cortex	t_c	[0.15, 0.65]	μm
Viscosity cortex	η_c	0.5	kPa·s
Active tension cortex	γ	[0, 0.9]	nN/μm
Bulk modulus cell	K	25	kPa
Liquid viscosity	η_l	5.0	Pa·s
Normal cell-pipette friction	λ^p_n	5.0	kPa·s/μm
Tangential cell-pipette friction	λ^p_t	0.1	kPa·s/μm
Cell radius	R	6	μm
Simulation timestep	Δt	0.75	ms
Maximal error conjugate gradient	F_{res}	1.0	pN
Number of mesh nodes per cell	N_v	2562	-
Pipette inner radius	R_p	3.5	μm
Pipette rounding radius	R_r	0.5	μm
Pipette stiffness	k_p	40	kPa·s/μm
Pressure increase rate	$\mathrm{d}\Delta P/\mathrm{d}t$	25	Pa/s

Micropipette Aspiration The micropipette is represented as a hollow cylinder, with a torus glued at the end, with a tube (rounding) radius $R_r = 0.5\,\mu\mathrm{m}$, and an inner radius (equal to the cylinder radius) of $R_p = 3.5\,\mu\mathrm{m}$ – see Fig. 2(a). An underpressure ΔP is applied on any node of the deformable cell that has crossed the center of the pipette's bounding torus. The aspiration force on the node is simply:

$$\boldsymbol{F}_i^{p,a} = \mathcal{A}_i \Delta P\, \hat{\boldsymbol{n}}_i, \tag{S30}$$

with $\mathcal{A}_i$ and $\hat{\boldsymbol{n}}_i$ the Voronoi area and normal associated with node i. Overlap with the pipette wall is prevented using a linear stiffness k_p. The contact force on the node is:

$$\boldsymbol{F}_i^{p,c} = k_p\, \mathcal{A}_i \delta_i^p\, \hat{\boldsymbol{n}}_c(\boldsymbol{x}_i), \tag{S31}$$

if overlap distance $\delta_i^p > 0$ and zero otherwise. $\hat{\boldsymbol{n}}_c(\boldsymbol{x}_i)$ is the normal direction of the pipette's inner surface at the position of node i. Both δ_i^p and $\hat{\boldsymbol{n}}_c$ can be trivially obtained from simple geometric considerations. We set $k_p = 40\,\mathrm{kPa}/\mu\mathrm{m}$, sufficiently high to prevent any meaningful overlap in the range of applied pressure. For nodes that are in contact with the pipette ($\delta_i^p > 0$), we include an additional contact drag force:

$$\boldsymbol{F}_i^{p,d} = -\Lambda_i^p\, \boldsymbol{v}_i, \tag{S32}$$

with friction tensor

$$\Lambda_i^p = \mathcal{A}_i \left[\lambda_n^p \hat{\boldsymbol{n}}_{ij} \hat{\boldsymbol{n}}_{ij}^T + \lambda_t^p \left(I - \hat{\boldsymbol{n}}_{ij} \hat{\boldsymbol{n}}_{ij}^T \right) \right],$$

where λ_n^p and λ_t^p are normal and tangential cell-pipette friction constants. We set $\lambda_n^p = 5\,\mathrm{kPas}/\mu\mathrm{m}$, sufficiently high to dampen numerical oscillations in the stiff potential k_p and $\lambda_t^p = 0.1\,\mathrm{kPas}/\mu\mathrm{m}$, sufficiently low to represent quasi-frictionless contact.

In the MA simulation, we start at $\Delta P = 0\,\mathrm{Pa}$, and gradually increase ΔP until the aspirated length $L_p = R_p$, i.e. the aspirated region forms a hemisphere in the micropipette. The current pressure at this point is registered as the critical pressure P_c. The rate of pressure increase must be sufficiently slow with respect to the viscous relaxation time of the cell. We set $\mathrm{d}\Delta P/\mathrm{d}t = 25\,\mathrm{Pa/s}$. The full set of parameters used to perform the MA simulations is listed in Table S1.

Dual Pipette Aspiration The DPA simulation consists of two subsequent steps: 1) Two cells are put in close proximity[3] and allowed to freely adhere until they equilibrate at a stable contact area and 2) We apply opposite pulling forces on both cells and register their separation. Hence, we do not represent the two micropipettes explicitly, but simply distribute a pulling force over the cell. To do this, we adopt two configurations:

A For the results in Fig. 3 and Fig. 4, we distribute the total force evenly over all nodes with a contact area equal to zero. Such a distribution is numerically more favorable, since it ensures a low excess force for each degree of freedom. In these simulations, we were only interested in the pull-off force, which was verified to be affected very little by the precise manner of force distribution.

B For Fig. 6, we must quantify the shape (R_a) and the geometry of the contact area (R_c). In order to compare to (7), we need to adopt their assumptions, which include that the pulling force is applied only at the top of the cell. Here, we selected the top 5% of mesh nodes at either side of the cell doublet, and distributed the pulling force evenly among them.

The purpose of configuration A is to measure the pull-off force. For this, we very slowly increase the applied force applied to the cells, and register the force at which rapid detachment of the cell-cell contact occurs. Using this setup, we can accurately quantify the pull-off force in one simulation, as long as the rate of applied force increase is much slower than the relaxation dynamics of the cell. We set $\mathrm{d}F/\mathrm{d}t = 0.25\,\mathrm{nN/s}$.

For configuration B, we perform a separate and independent simulation for each applied force F. To ensure that a stable configuration is reached, we simulate until either the two cells have been fully separated, or until a pulling time of $60\,\mathrm{s}$ has passed. After this, the current contact area A_c between the two cells is registered, and a corresponding contact radius $R_c = \sqrt{A_c/\pi}$. To obtain a robust estimate of the apical radius R_a, we follow the following procedure:

I Obtain the contact axis $\hat{\boldsymbol{n}}_{AB}$ for cells A and B as:

$$\hat{\boldsymbol{n}}_{cc} = \frac{1}{A_{c,A} + A_{c,B}} \left(\sum_{\forall i \in A} A_{c,i} \hat{\boldsymbol{n}}_i - \sum_{\forall i \in B} A_{c,i} \hat{\boldsymbol{n}}_i \right),$$

where $A_{c,i}$ is the contact area and $\hat{\boldsymbol{n}}_i$ the surface normal vector of node with index i.

[3] The cells must be at least within their adhesive range h_0 so that the adhesion process may start.

Table S2: Complete list of parameters used to simulate the DPA experiments in shown in Fig. 3. Square brackets indicate ranges of parameters that were varied across multiple simulations.

Parameter	**Symbol**	**Value(s)**	**Units**
Young's modulus cortex	E_c	30	kPa
Normal contact stiffness	$E_{c,c}$	30	kPa
Poisson's ratio cortex	ν_c	1/3	-
Thickness cortex	t_c	[0.15, 2.5]	µm
Viscosity cortex	η_c	2.67	kPa·s
Active tension cortex	γ	[0, 1.5]	nN/µm
Bulk modulus cell	K	30	kPa
Liquid viscosity	η_l	1.0	Pa·s
Normal cell-cell friction	λ_n	0.05	kPa·s/µm
Tangential cell-cell friction	λ_t	0.05	kPa·s/µm
Cell-cell adhesion	w	0.25	nN/µm
Effective range of adhesion	h_0	50	nm
Cell radius	R	10	µm
Simulation timestep	Δt	0.5	ms
Maximal error conjugate gradient	F_{res}	5.0	pN
Number of mesh nodes per cell	N_v	2562	-
Rate of force increase	$\mathrm{d}F/\mathrm{d}t$	0.25	nN/s

Table S3: Complete list of parameters used to simulate the DPA experiments shown in Fig. 4 and Fig. 6. Square brackets indicate ranges of parameters that were varied across multiple simulations.

Parameter	**Symbol**	**Value(s)**	**Units**
Young's modulus cortex	E_c	[5, 35]	kPa
Normal contact stiffness	$E_{c,c}$	100	kPa
Poisson's ratio cortex	ν_c	1/3	-
Thickness cortex	t_c	[0.15, 0.65]	µm
Viscosity cortex	η_c	2.67	kPa·s
Active tension cortex	γ	[0, 0.9]	nN/µm
Bulk modulus cell	K	30	kPa
Liquid viscosity	η_l	1.0	Pa·s
Normal cell-cell friction	λ_n	0.05	kPa·s/µm
Tangential cell-cell friction	λ_t	0.05	kPa·s/µm
Cell-cell adhesion	w	[0.05, 0.9]	nN/µm
Effective range of adhesion	h_0	50	nm
Cell radius	R	6	µm
Simulation timestep	Δt	1.0	ms
Maximal error conjugate gradient	F_{res}	5.0	pN
Number of mesh nodes per cell	N_v	[2562, 10242]	-

II Obtain the center of the contact $\boldsymbol{x}_{cc}$ by integrating:

$$\boldsymbol{x}_{cc} = \frac{1}{A_{c,A} + A_{c,B}} \left(\sum_{\forall i \in A} A_{c,i} \hat{\boldsymbol{x}}_i - \sum_{\forall i \in B} A_{c,i} \hat{\boldsymbol{x}}_i \right).$$

III For each node i, compute the distance r_i to the line defined by $\boldsymbol{x}_{cc}$ and $\hat{\boldsymbol{n}}_{cc}$.

IV For each node i, compute the (positive) distance x_i along the line defined by $\boldsymbol{x}_{cc}$ and $\hat{\boldsymbol{n}}_{cc}$.

V Sort each node i in one of 25 bins along the central axis according to x_i.

VI Compute the average radius r_i for each bin k:

$$r_k = \frac{1}{N_k} \sum_{\forall i \in k} r_i.$$

Table S4: Complete list of simulation parameters used to simulate the optical trap experiments shown in Fig. 5.

Parameter	**Symbol**	**Value(s)**	**Units**
Young's modulus cortex	E_c	15	kPa
Normal contact stiffness	$E_{c,c}$	100	kPa
Poisson's ratio cortex	ν_c	1/3	-
Thickness cortex	t_c	0.3	µm
Viscosity cortex	η_c	2.67	kPa·s
Active tension cortex	γ	0.4	nN/µm
Bulk modulus cell	K	30	kPa
Liquid viscosity	η_l	1.0	Pa·s
Normal cell-substrate friction	$\lambda_{n,s}$	0.15	kPa·s/µm
Tangential cell-substrate friction	$\lambda_{t,s}$	0.15	kPa·s/µm
Tangential cell-bead friction	$\lambda_{t,b}$	0.20	kPa·s/µm
Tangential cell-bead friction	$\lambda_{t,b}$	0.20	kPa·s/µm
Cell-bead adhesion	w	0.517	nN/µm
Effective range of adhesion	h_0	50	nm
Cell radius	R	7	µm
Patch size	L_p	10	µm
Bead radius	R_b	1.8	µm
Simulation timestep	Δt	2.0	ms
Maximal error conjugate gradient	F_{res}	5.0	pN
Number of mesh nodes per cell	N_v	10242	-

VII The maximal r_k is recorded as the apical radius: $R_a = \max(r_k)$

Fig. S3 illustrates this procedure for a specific cell configuration. The maximum of the black line gives the apical radius R_a.

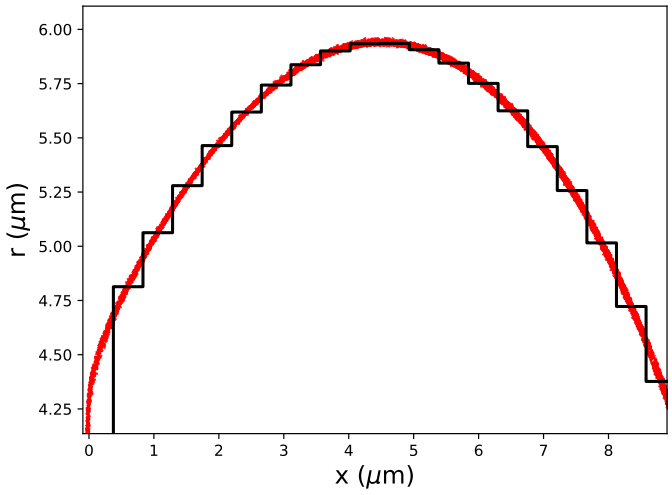

Figure S3: Illustration of algorithm to robustly compute the apex radius R_a: node positions (red dots) are collected in axial bins, based on the distance to the contact plane. For each axial bin (25 in total), the average distance to the axis is computed. The maximal of these values gives the apical radius R_a. In the shown configuration, we can estimate $R_a \approx 5.9\,\mu\text{m}$.

Optical tweezers To replicate an optical tweezers experiment in a simulation, we create a surface for the cell to spread on which is composed of two 'patches'. A central, rectangular patch of $10\,\mu\text{m} \times 10\,\mu\text{m}$ (indicated in green in Fig. 5) has a very high adhesion energy, while the surrounding patch (indicated in black in Fig. 5) has no adhesion. We set the adhesion energy between cell and substrate $w_{c,s}$ to $0.8\,\text{nN}/\mu\text{m}$, sufficiently high to ensure that the full patch will be covered by the cell. The cell radius was slightly increased (from $6\,\mu\text{m}$ to $7\,\mu\text{m}$) to be consistent with the results shown in (8). Next, we let the cell adhere to the surface until its positions equilibrate (Fig. 5 top left). In a second phase, we relax all elastic stresses (assuming

that the spreading could occur over a long timescale), and let a bead adhere to the side of the cell, at the height where it maximally protrudes. The adhesion energy between cell and bead $w_{c,b}$ is tuned so that the experimentally observed contact radius is approximated. Finally, we apply various pulling forces to the bead and record the displacement of the bead. Each simulation is repeated for 5 random orientations of the cell (to artifacts due to mesh coarseness near the cell-bead contact area). The slope of displacement with respect to pulling force is used to estimate an apparent Young's modulus of the cell. The full Table of simulation parameter used for this experimental setup is shown in Table S4.

Parameter choice As mentioned in 'Computational Model', a requirement for the applied contact model to be valid is that the normal elastic compression is sufficiently small compared to the cortex thickness. For Fig. 3, we have ensured this by choosing a sufficiently high E_c and a sufficiently low w when varying the thickness t_c over a wide range (parameters listed in Table S2). On the other hand, for our estimated parameters of the S180 cell, the elastic modulus of the cortex is relatively low ($\approx$ 15 kPa) and the thickness is very small ($\approx$ 0.3 μm). In this case, when adhesion w is high, the Hertzian assumptions are violated. However, in these cases the normal elastic compression (which is always $\ll t_c$), is negligible compared to the total deformation of the cell. Thus, we can safely and without loss of accuracy increase the effective stiffness of the contact model $E_{c,c} > E_c$, so that large and incorrectly computed overlap distances are prevented. The full set of parameters to simulate these configurations is listed in Table S3. The sub-set of this table that contains our estimates for S180 cells was provided in Table 1.

Aside from the parameters that extensively discussed in the main manuscript (E_c, ν_c, t_c, γ), the numerical simulations require some additional parameters. Since we solve a dynamic system, the forces on the right hand side are balanced by viscosities / damping forces. These viscosities do not influence the steady-state results discussed in the main manuscript, but are required for the numerical convergence. The order of magnitude of these viscosities is chosen in the range of estimates for real biological cells (i.e. kPa·s/μm for cell-cell frictions and kPa·s for cortex viscosity (13)). The simulation time step is varied based on the specific simulation setup (from $0.5\,\mathrm{ms}$ to $2\,\mathrm{ms}$). The Conjugate Gradient solver was assigned the convergence criterion of a maximal force residual of 5 pN.

References

1. Odenthal T, et al. (2013) Analysis of initial cell spreading using mechanistic contact formulations for a deformable cell model. *PloS Comp Biol* 9(10): e1003267.
2. Guyot Y, et al. (2016). Immersed Boundary Models for Quantifying Flow-Induced Mechanical Stimuli on Stem Cells Seeded on 3D Scaffolds in Perfusion Bioreactors. *PLoS Comp Biol* 12(9) e1005108.
3. Johnson KL, Greenwood JA (1997) An adhesion map for the contact of elastic spheres. *J. Colloid Interface Sci* 192(2): 326-333.
4. Van Gelder A (1998) Approximate Simulation of Elastic Membranes by Triangulated Spring Meshes. *Journal of Graphics Tools* 3(2): 21–41.
5. Helfrich W (1973) Elastic properties of lipid bilayers: theory and possible experiments. *Verlag der Zeitschrift für Naturforschung* 28(11-12): 693–703.
6. Kot M, Nagahashi H, Szymczak P (2015) Elastic moduli of simple mass spring models. *Visual Computer* 31(10): 1339–1350.
7. Brochard-Wyart F, de Gennes PG (2003) Unbinding of adhesive vesicles. *C.R. Phys* 4, 281.
8. Al Kilani A, et al. (2011) Negative Feedback from Integrins to Cadherins: A Micromechanical Study. *Biophys J* 101: 336 – 344.
9. Van Liedekerke P, et al. (2013) Solving microscopic flow problems using stokes equations in sph. *Comp Phys Comm* 184: 1686–1696.
10. Guennebaud G, Benoît J, et al. (2010) Eigen v3. *http://eigen.tuxfamily.org*.
11. He K, Dong S, and Zhou Z (2007). Multigrid contact detection method. *Physical Review E* 75(3): p.036710.
12. Dunavant DA (1985) High degree efficient symmetrical Gaussian quadrature rules for the triangle. *International Journal for Numerical Methods in Engineering* 21(6): 1129 – 1148.
13. Bausch AR, et al. (1998) Local Measurements of Viscoelastic Parameters of Adherent Cell Surfaces by Magnetic Bead Microrheometry. *Biophys J* 75: 2038 – 2049.
14. Seifert U, Lipowsky R (1995) Morphology of vesicles. *Handbook of biological physics* 1: 403 – 464.

3 Supplementary Figures

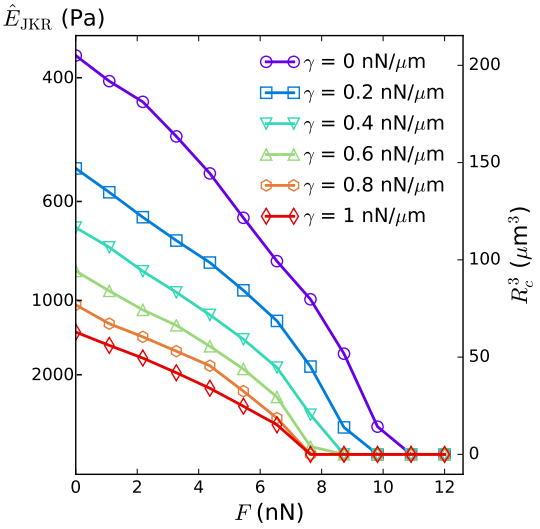

Figure S4: Cube of the contact radius R_c^3 as a function of pulling force F with varying active tension γ for cell mechanical properties in Table 1. The axis on the left hand side indicates the equivalent combined JKR modulus that yields the corresponding contact radius at zero loading ($F = 0$), computed using Eq. (5). Active tension has the effect of greatly increasing the apparent stiffness of the cell.

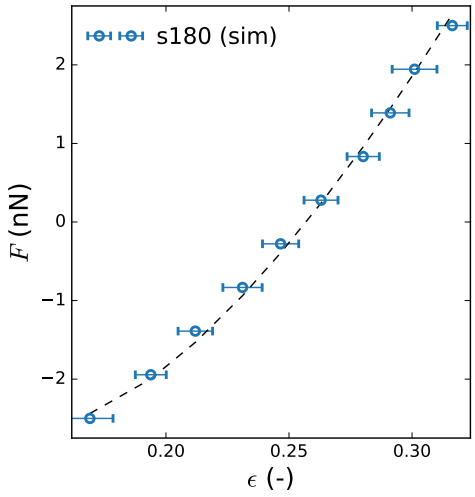

Figure S5: Simulation of cell compression between two rigid parallel plates. The cell has been assigned the parameters from Table S3, with $w = 0.3\,\mathrm{nN/\mu m}$ for both top and bottom plate and with $N_v = 2562$. Next, a compressive (positive) or tensile (negative) force F is applied on the top plate and the system is allowed to equilibrate. The final distance between the plates Δz is registered to compute the strain $\epsilon = (2R - \Delta z)/2R$, and this for five independent configurations, where we have rotated our initial mesh to random orientations, to prevent discretization artifact. The error bars show the standard deviation among these initial orientations. The dashed line shows a fit of $F \sim \epsilon^{3/2}$ to demonstrate the Hertzian response of the highly deformed cell.

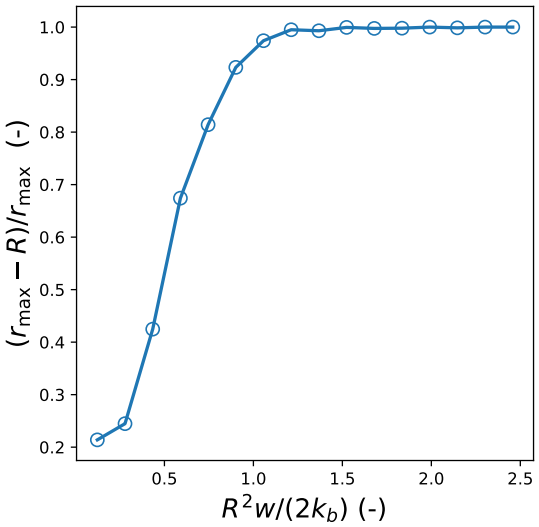

Figure S6: Comparison of deformable cell model cell spreading simulation with adhesion criterion $w = 2k_b/R^2$ for idealized vesicles (14). The limit of ideal vesicles (no volume change, no area change) is approached by setting $E_c = 100\,\mathrm{kPa}$, $t_c = 250\,\mathrm{nm}$ and $\gamma = 0\,\mathrm{nN/\mu m}$. This plot shows the degree of 'flatness' as a function of normalized adhesion energy with $r_{\max}$ the maximal radius of curvature. For $R^2w/(2k_b) < 1$, no flattened area is present because adhesion is insufficient to counteract the local bending resistance. Adhesion here only exists due to the finite adhesive range h_0. For $R^2w/(2k_b) > 1$, adhesion is able to overcome the bending resistance and establish a flattened contact area.

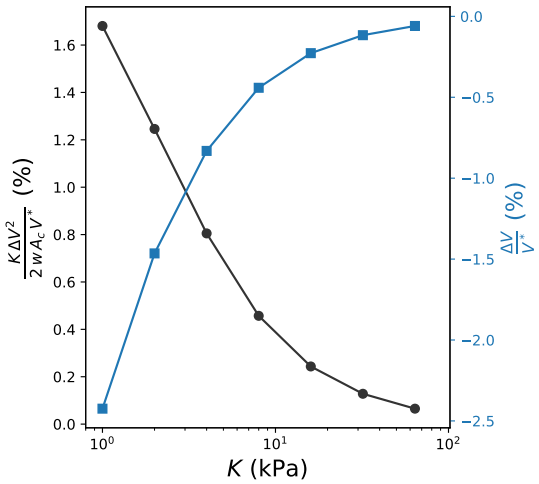

Figure S7: Influence of bulk modulus K in a simulated cell spreading experiment using parameters from Table 1. Black: Ratio of total hydrostatic energy $\frac{1}{2}K\Delta V^2/V^*$ and total adhesion energy $w\,A_c$ (contact area A_c) for varying cell bulk modulus K, using parameters from Table 1, and $w = 0.2\,\mathrm{nN/\mu m}$. The mechanical energy stored in hydrostatic compression decreases with increasing K, but its mechanical contribution relative to adhesion energy is small, even for small K. Blue: Relative change of the cells' volume for varying K.

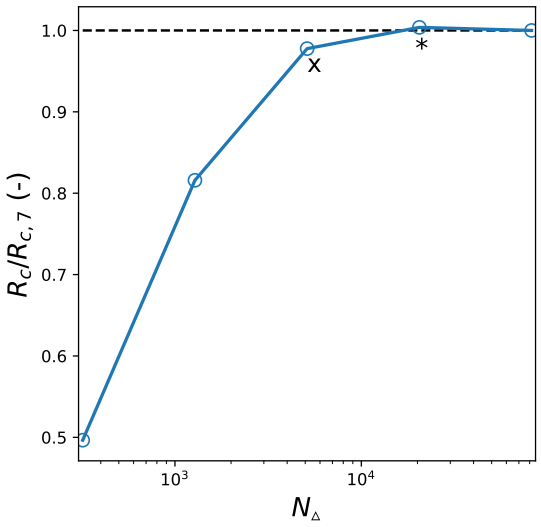

Figure S8: Contact radius as a function of number of triangles N_Δ of the triangulated mesh that represents the cell, for a cell spreading simulation with parameters from Table 1, and $w = 0.2\,\mathrm{nN/\mu m}$. The final contact radius R_c after cell spreading is shown relative to the contact radius of the most refined mesh $R_{c,7}$, which has 40,962 vertices and 81,920 triangles. The refinements used in this study are indicated with symbols: $N_\Delta^\times = 5{,}120$; $N_\Delta^* = 20{,}480$.

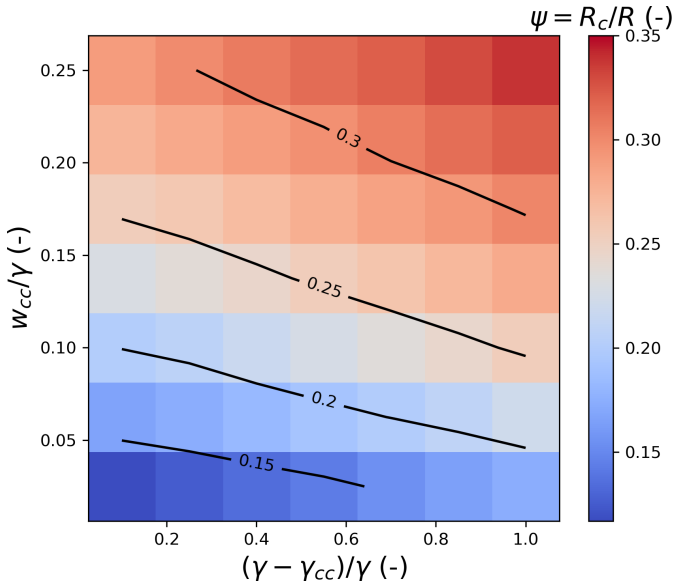

Figure S9: Relative contribution of cell-cell adhesion energy w_{cc} and differential interfacial tension $(\gamma - \gamma_{cc})/\gamma$ with γ_{cc} the active tension in the cell-cell contact region, to the radius of contact of an adhering cell doublet. Each 'pixel' represents an individual simulation with $E_c = 15\,\mathrm{kPa}$, $t_c = 0.3\,\mu\mathrm{m}$ $\gamma = 1.0\,\mathrm{nN/\mu m}$, where γ_{cc} and w_{cc} were varied as indicated.

Table S5: Summary of a linear model of relative contact area $\frac{A_c}{4\pi R^2} \sim a_0 + a_1 \frac{\gamma_{cc}}{\gamma} + a_2 \frac{w_{cc}}{\gamma}$ for a simulated cell-cell adhesion simulation (Fig. S9) with E_c =15 kPa, $t_c = 0.3\,\mu\text{m}$, $\gamma = 1.0\,\text{nN}/\mu\text{m}$, and varying cell-cell adhesion energy w_{cc} and cortical tension at the cell-cell interface γ_{cc}. Obtained parameter estimates are $a_0 = 0.0004 \pm 0.001$, $a_1 = 0.0275 \pm 0.001$ and $a_2 = 0.3449 \pm 0.005$ Data automatically generated by *statsmodels* in Python.

Dep. Variable:	contact area	**R-squared:**	0.993
Model:	OLS	**Adj. R-squared:**	0.992
Method:	Least Squares	**F-statistic:**	3049.
Date:	Fri, 23 Nov 2018	**Prob (F-statistic):**	1.29e-49
Time:	16:13:18	**Log-Likelihood:**	226.91
No. Observations:	49	**AIC:**	-447.8
Df Residuals:	46	**BIC:**	-442.2

	coef	**std err**	**t**	**P>|t|**	**[95.0% Conf. Int.]**
Intercept	0.0004	0.001	0.423	0.674	-0.002 0.002
gammacc	0.0275	0.001	23.737	0.000	0.025 0.030
adhesion	0.3449	0.005	74.393	0.000	0.336 0.354

Omnibus:	6.291	**Durbin-Watson:**	0.991
Prob(Omnibus):	0.043	**Jarque-Bera (JB):**	6.036
Skew:	-0.859	**Prob(JB):**	0.0489
Kurtosis:	2.952	**Cond. No.**	15.6